ADVANCED
SCIENCE NEWS
www.advancedsciencenews.com

NANO MICRO
small

Perovskite Solar Cells

Broadband Light Absorption and Efficient Charge Separation Using a Light Scattering Layer with Mixed Cavities for High-Performance Perovskite Photovoltaic Cells with Stability

Byeong Cheul Moon, Jung Hyo Park, Dong Ki Lee, Nikolai Tsvetkov, Ilwoo Ock, Kyung Min Choi, and Jeung Ku Kang**

$CH_3NH_3PbI_3$ *is one of the promising light sensitizers for perovskite photovoltaic cells, but a thick layer is required to enhance light absorption in the long-wavelength regime ranging from PbI_2 absorption edge (500 nm) to its optical band-gap edge (780 nm) in visible light. Meanwhile, the thick perovskite layer suppresses visible-light absorption in the short wavelengths below 500 nm and charge extraction capability of electron–hole pairs produced upon light absorption. Herein, we find that a new light scattering layer with the mixed cavities of sizes in 100 and 200 nm between transparent fluorine-doped tin oxide and mesoporous titanium dioxide electron transport layer enables full absorption of short-wavelength photons ($\lambda < 500$ nm) to the perovskite along with enhanced absorption of long-wavelength photons (500 nm $< \lambda < 780$ nm). Moreover, the light-driven electric field is proven to allow efficient charge extraction upon light absorption, thereby leading to the increased photocurrent density as well as the fill factor prompted by the slow recombination rate. Additionally, the photocurrent density of the cell with a light scattering layer of mixed cavities is stabilized due to suppressed charge accumulation. Consequently, this work provides a new route to realize broadband light harvesting of visible light for high-performance perovskite photovoltaic cells.*

B. C. Moon, Dr. J. H. Park, Dr. D. K. Lee,
Dr. N. Tsvetkov, I. Ock, Prof. J. K. Kang
Graduate School of Energy, Environment, Water, and
Sustainability (EEWS)
Department of Materials Science and Engineering
Korea Advanced Institute of Science
and Technology (KAIST)
291 Daehak-ro, Yuseong-gu, Daejeon 34141, Republic of Korea
E-mail: jeungku@kaist.ac.kr
Prof. K. M. Choi
Department of Chemical and Biological Engineering
Sookmyung Women's University
100 Cheongpa-ro 47 gil, Yongsan-gu, Seoul 04310, Republic of Korea
E-mail: kmchoi@sookmyung.ac.kr

One of the main challenges facing humanity is to overcome the problems related to emission of carbon dioxide in the atmosphere of the earth, especially those related to severe climate change. The photovoltaic conversion of abundant solar energy into electric energy could provide a sustainable solution to this challenge, and in this light a novel architecture enabling efficient solar energy harvesting warrants attention as it would enable the development of more efficient photovoltaic cells. Perovskite photovoltaic cells,[1–4] which can harvest light using an organometal halide perovskite sensitizer, have shown promising optical properties such as a high extinction coefficient,[5] a long charge carrier diffusion length,[6] and a low-exciton (electron–hole pair) binding energy,[7] in addition to a straightforward synthetic route.[8] The $CH_3NH_3PbI_3$ perovskite is regarded as a superior

sensitizer for ultraviolet (UV) and visible lights compared to conventional sensitizers,[5] and it is also found to enable harvesting of solar energy via the two distinguished mechanisms.[9] One is attributed to the surface charge generation in the Beer–Lambert regime giving high extinction coefficients for photons in the short-wavelength region of $\lambda < 500$ nm that matches with the light-absorption edge by PbI_2 in the $CH_3NH_3PbI_3$ perovskite. In principle, this perovskite layer up to a thickness of about 200 nm enables to absorb the full spectrum photons in the short-wavelength region below 500 nm.[10] The other mechanism is related to the light absorption in the cavity regime ranging from the PbI_2 light-absorption edge (500 nm) to its optical band-gap edge (780 nm) and it occurs by the optical interference attributed to the volume charge generation between the junctions. For convenience, these imply that one could define the visible-light spectra for the $CH_3NH_3PbI_3$ perovskite into a short-wavelength region ($\lambda < 500$ nm) and a long-wavelength region (500 nm $< \lambda <$ 780 nm) depending on different light-absorption mechanisms. However, the long-wavelength regime requires a thick perovskite layer to enable full absorption of long-wavelength photons because its extinction coefficient for light absorption is smaller than even a half for that in the short-wavelength regime.[11] Meanwhile, increasing the thickness of the perovskite layer for enhanced absorption of long-wavelength photons limits visible-light absorption in the short-wavelength regime and also depresses charge extraction capability of electron–hole pairs generated upon light absorption.[12,13] Thus, optimizing the thickness of the perovskite layer to trade off efficient light absorption against charge separation remains one of the obstacles to realize high-performance perovskite photovoltaic cells.[14–28] In efforts to enable efficient light harvesting, light management[14] has been carried out for conventional thin film[15–17] and dye-sensitizing[18–20] photovoltaic cells. It is also notable that nanostructures of various geometries to control light trapping,[21,22] light scattering,[23,24] and localized surface plasmon resonance[25–28] have been developed on perovskite photovoltaics. In this light, a novel architecture that enables broadband absorption of short- and long-wavelength photons for visible light along with efficient charge separation of electron–hole pairs upon light absorption would pave a route to realize a new paradigm in perovskite photovoltaic cells.

Herein, we report a new light scattering layer (SCL) having mixed pore cavities of 100 and 200 nm in sizes between fluorine-doped tin oxide (FTO) and mesoporous titanium dioxide (m-TiO_2) electron transport layers. This SCL having mixed cavities (SCL-MIX) is a promising solution to overcome the limitations of perovskite

photovoltaic cells by fabricating cavities rather than adding the scattering material to induce photonic resonance in the perovskite absorber. The combined study of experiments and optical simulations demonstrates that SCL-MIX enables full absorption of short-wavelength photons within the perovskite layer with enhanced absorption of long-wavelength photons. Moreover, it has been shown that the light-driven electromagnetic (EM) field is built in the SCLs. This in turn allows efficient charge extraction from electron–hole pairs generated upon light absorption, thereby leading to increased photocurrent density as well as a higher fill factor (FF) resulting from the slow recombination rate. Additionally, efficient and fast electron extractions driven by the built-in EM field with SCL-MIX yield significantly suppressed charge accumulation and improved stability on photovoltaic cells.

A perovskite photovoltaic cell with the SCL is schematically shown in **Figure 1**A. The SCLs were prepared using a template-assisted fabrication method. First, the colloidal polystyrene nanospheres were filled with the titanium dioxide precursor and subsequently calcinated to make the SCL on pore cavities (Figure S1, Supporting Information). The mesoporous titanium dioxide (m-TiO_2) layer was then deposited onto the SCL and the cross-sectional scanning electron microscope (SEM) image for the layer of cavities
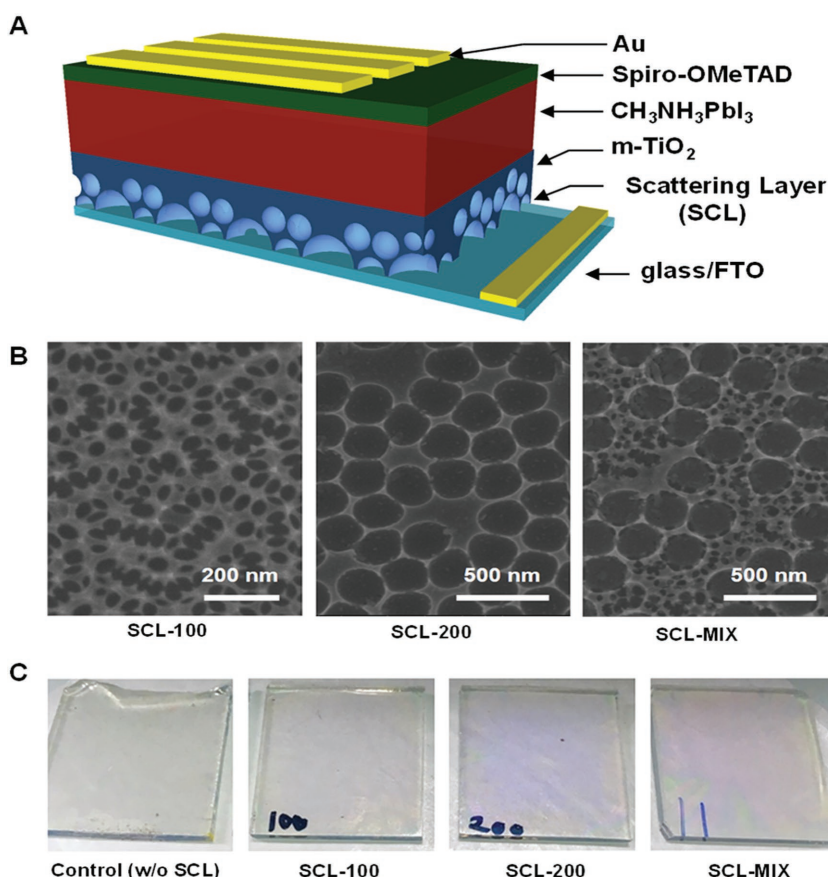

Figure 1. A) Schematic illustration of the $CH_3NH_3PbI_3$ perovskite photovoltaic cell with the scattering layer of mixed cavities (SCL-MIX). B) Surface SEM images for SCL-100, SCL-200, and SCL-MIX structures. C) Pictures of m-TiO_2 films prepared on the glass/FTO/SCLs substrate presenting variations in color due to light scattering.

has been obtained as shown in Figure S2 (Supporting Information). These two layers serve as a channel for transport of electrons extracted from the perovskite layer to the FTO, while the spiro-OMeTAD deposited on the other side of the perovskite layer provides a channel for hole transport to the Au layer. In addition, the field-emission scanning electron microscope (FE-SEM) images of Figure 1B show the surface morphologies of SCLs corresponding to SCL-100, SCL-200, and SCL-MIX. SCL-100 and SCL-200 have monodispersed and round cavities with average diameters of 100 and 200 nm, respectively, while SCL-MIX has mixed cavities of 100 and 200 nm. Moreover, Figure S3 (Supporting Information) presents X-ray diffraction (XRD) patterns for SCL-100, SCL-200, and SCL-MIX in the anatase TiO_2 phase. Figure 1C shows the appearance of the fabricated samples with no SCL, SCL-100, SCL-200, and SCL-MIX. And the films having SCLs became to blurry but dim purple in color. The variation in color implies that the light is scattered in the presence of cavities of SCLs, and this is corroborated by the decreased optical transmittance of the films under UV–visible light in Figure S4 (Supporting Information). Subsequently, optical simulations using a finite-difference time-domain (FDTD) method along with experiments were performed to clarify the mechanisms of SCL-100, SCL-200, and SCL-MIX for broadband absorption of visible light.

The optical simulations for absorption density (P_{abs}) on the $SCL/m\text{-}TiO_2/CH_3NH_3PbI_3$ architecture in the short-wavelength region of visible light are described in Figure S5 (Supporting Information) and the absorption density per unit volume (P_{abs}) is defined by the following equation of:

$$P_{abs} = -0.5\omega |E|^2 \,\text{Im}(\varepsilon) \qquad (1)$$

where ω is the angular frequency, E is the electric field, and $\text{Im}(\varepsilon)$ is the imaginary value of a complex permittivity for the material,[29,30] and the modeling details are described in the optical simulation section. In the short-wavelength region, the cells for control (w/o SCL) and SCL-100 show linear gradient absorption profiles along the y-direction parallel to the direction of the incident plane-wave light source. Meanwhile, those for SCL-200 and SCL-MIX show that the incident light is absorbed through the dispersive direction from the interface of the $m\text{-}TiO_2$ and the perovskite layers. This implies that SCL-200 and SCL-MIX could cause scattering of the photons to the perovskite layer, thereby leading to enhanced absorption of photons in the short-wavelength region for perovskite photovoltaic cells.

We also found that the light-absorption density on the $SCL/m\text{-}TiO_2/CH_3NH_3PbI_3$ architecture is enhanced in the long-wavelength region (500 nm < λ < 800 nm). **Figure 2**A shows that light absorption is concentrated on the interface of $m\text{-}TiO_2$ with the perovskite layer in the control (w/o SCL) configuration, while the absorption density in the perovskite layer decreases rapidly with maximum absorption density of 8.89×10^{12} near the interface. However, the absorption profiles in Figure 2B,C with the SCL-100 and SCL-200 configurations prove that their light-absorption density at the interfaces of the perovskite layer are enhanced by 23% and 17%, respectively, compared to that with the control configuration. Figure 2D further demonstrates that SCL-MIX causes the light to be absorbed into the dispersive direction from the interface of the perovskite layer with significantly enhanced absorption of 70%. This implies that the SCL composed of the mixed cavities is exceptionally effective in enabling absorption of the long-wavelength photons (λ > 500 nm) in visible light. When the size of a cavity is comparable with the
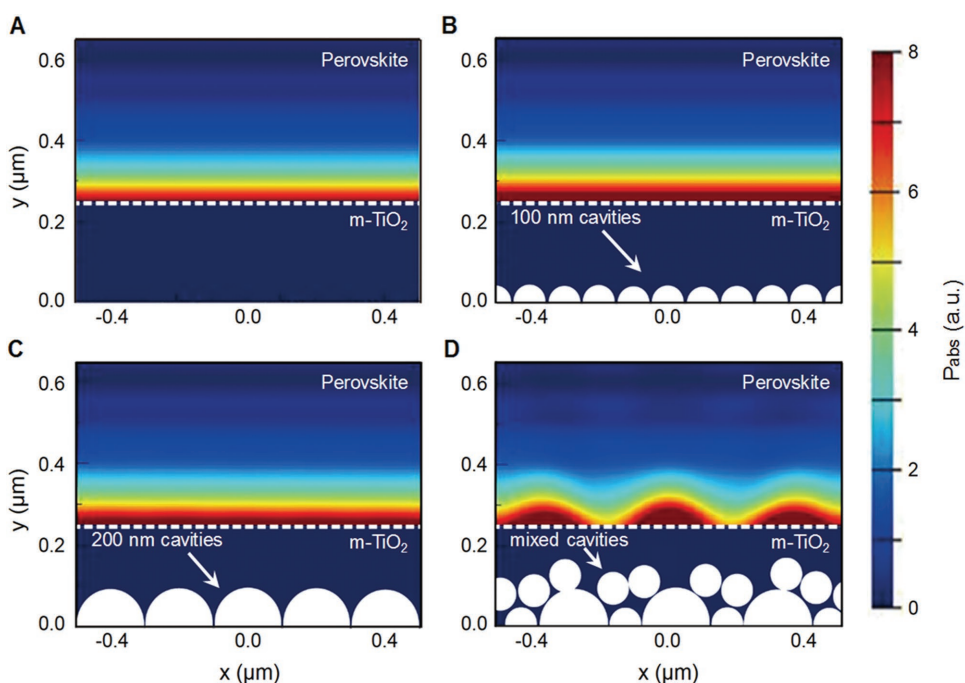

Figure 2. The spatial distribution of the light-absorption density (P_{abs}) with the $SCL/m\text{-}TiO_2/CH_3NH_3PbI_3$ architecture for A) control (w/o SCL), B) SCL-100, C) SCL-200, and D) SCL-MIX, where the incident plane wave of 500 nm < λ < 800 nm is given along the y-axis.

wavelength of visible light, the light scattering wavelength (λ_s) relies on the nondimensional size parameter (α) of the scattering cavity, which is defined by a ratio of its dimension to the scattering wavelength according to the following relation of:

$$\lambda_s = 2\pi r / \alpha \qquad (2)$$

where r is the effective radius of the scattering cavity. The cell with SCL-MIX results in closely packed mixed cavities with intimate connections. When the interparticle spacing becomes smaller, two neighboring individual particles would behave like a single particle of the larger size, which is referred to as the dual-particle coupling effect.[27] Thus, closely neighboring cavities lead to an increase in the effective radius (r) of the scattering cavity compared to that of a single cavity corresponding to $r = 50$ or 100 nm, while it leads to a decrease in the size parameter (α) due to distortion of the apparent shape of cavities from a sphere ($\alpha = 1$). Thus, the efficient scattering of long-wavelength photons by SCL-MIX is attributed to the increased scattering wavelength (λ_s) by the size and shape of the cavities. However, the light–matter interactions for scattering and absorption rely not only on the sizes of the cavity but also on the spacing between cavities.[27] When two different sized polystyrene spheres are mixed to form a layer, the packing density of the spheres is higher than that of a layer consisting of monosized spheres. The denser packing of polystyrene spheres leads to the smaller interparticle

spacing of these spheres, thereby leading to the narrower gaps between the cavities of SCL-MIX while boosting light absorption in the perovskite via stronger coupling resonance. Consequently, SCL-MIX shows a remarkable enhancement of the P_{abs} value through the phonic resonance induced by the small spacing between cavities as well as the size parameter of the cavities resulting from dual-particle coupling.

Optical absorption and steady-state photoluminescence (PL) spectroscopy and photovoltaic characterizations also have been utilized to determine the light-absorption properties with SCL-100, SCL-200, and SCL-MIX. The visible-light absorbance spectra presented in Figure S6 (Supporting Information) show that the absorption of the perovskite layer in the long-wavelength region is improved by the SCLs compared to that of the control cell. Additionally, the light-harvesting efficiency (LHE) spectra in **Figure 3**A provide a clear evidence that the perovskite layer of the control cell with a thickness of 400 nm lends low LHE in the long-wavelength region, whereas almost 100% absorption is feasible only in the short-wavelength region. Meanwhile, SCL-MIX provided the most efficient harvesting of photons in the long-wavelength region, consistent with the optical simulation results obtained by using the FDTD method, so that SCL-MIX was also found to give increased absorption of photons in the short-wavelength region. Furthermore, the steady-state PL spectra obtained with a 514 nm laser (Figure 3B) verify that the normalized PL emission peak at ≈760 nm corresponding to the band gap of the perovskite is significantly increased for SCL-MIX through enhanced absorption. Moreover, a
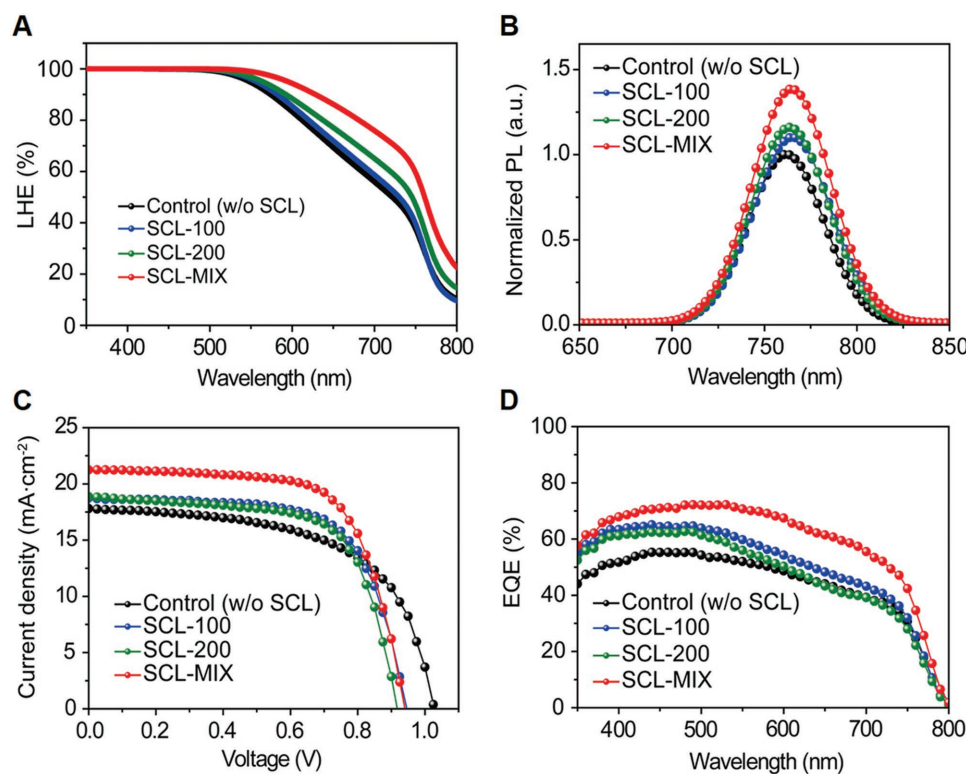

Figure 3. A) Light-harvesting efficiency (LHE) and B) steady-state PL spectra for photovoltaic cells with control (w/o SCL) and SCL-100, SCL-200, and SCL-MIX, where LHE is calculated with the equation of LHE (%) = $(1 - R)(1 - 10^{-ABS})$ with R and ABS denoting the reflectance and the absorbance of the perovskite absorber, respectively. C) J–V curves and D) EQE spectra for corresponding photovoltaic cells.

red shift of the PL peaks was observed for the perovskite films with SCLs. This shift is attributed to the built-in electric field at the interface of the m-TiO$_2$/perovskite and the SCL. It is notable that the SCL could lead to the Stark shift in the PL spectra of the perovskite layer.[31,32] Figure 3C also shows the photovoltaic J–V characteristics for the perovskite photovoltaic cells, and their photovoltaic device parameters are summarized in Table S1 (Supporting Information). To fabricate photovoltaic cells having SCL-MIX, we have also conducted the optimization experiments for determining the mixing ratio of small cavities to large cavities in the SCLs by changing the percentages of large cavities, as shown in Figure S7 (Supporting Information). The measured power conversion efficiency of 13.5% with SCL-MIX is determined to be significantly higher than 10.8% with the control (w/o SCL) configuration. Moreover, the photovoltaic cell with SCL-MIX showed the highest J–V performance with a significant improvement of short circuit current density (J_{sc}). It is notable that the presence of the SCL-100 and SCL-200 also leads to an increase of both the J_{sc} and the FF. Additionally, the external quantum efficiency (EQE) spectra in Figure 3D show that SCL-MIX leads to a broadband absorption of visible light. The highest J_{sc} of 21.2 mA cm^{-2} with SCL-MIX was obtained via broadband absorption of short- and long-wavelength photons in visible light, while SCL-100 and SCL-200 showed small enhancements of light absorption. Meanwhile, a decrease in open-circuit voltage (V_{oc}) of a photovoltaic cell with the SCLs is attributed to the rough interface between m-TiO$_2$ and FTO, as shown in the increased series resistance (R_s). Furthermore, we have conducted control experiments and simulations to investigate the effect of the thickness for SCLs with mono-, double-, and triple-layers on scattering. The optical simulation in Figure S8 (Supporting Information) demonstrates that the increase in the thickness of the SCL

does not lead to a significant change in the light absorption into the perovskite layer. Also, the experimental measurements in Figure S9 (Supporting Information) clarify that the thickness of the SCLs does not result in a significant effect on the current density while its leading to decrease of the open-circuit voltage for a photovoltaic cell.

Moreover, we have carried out a FDTD simulation for the EM field density[23] in the SCL/m-TiO$_2$/perovskite configuration. To elucidate the role of the SCL in giving the light-driven EM field distribution, the plane EM wave ranging from 500 to 800 nm, which includes the long-wavelength region, enters into the y-direction, and the resulting EM field distribution profiles are shown in **Figure 4**. In the EM field distribution, there are two resonance modes, which include the bulk resonance mode induced by coupling of TiO$_2$ and perovskite films as well as the cavity resonance mode induced by cavities.[21,27] The bulk resonance exists for all of the cell configurations both at the surface of m-TiO$_2$ and at the interface between m-TiO$_2$ and perovskite materials, whereas the cavity resonance is observed near the cavities and it depends on the cavity size and the spacing between cavities. Figure 4A indicates that only the bulk resonance exists, resulting in the weak light-driven standing waves. However, as shown in Figure 4B–D, light-driven standing waves near the cavities become stronger due to the cavity resonance. Because the cavity resonance depends on the cavity size, only a small improvement is observed for SCL-100 in the long-wavelength light range. For SCL-200 and SCL-MIX, a stronger standing wave is found at the space between cavities but the magnitude for SCL-MIX is much higher due to its smaller spacing between cavities. The EM field distribution for the short-wavelength region is also shown in Figure S10 (Supporting Information), and the SCL-MIX showed the fourfold enhancement in the standing wave. These results indicate that
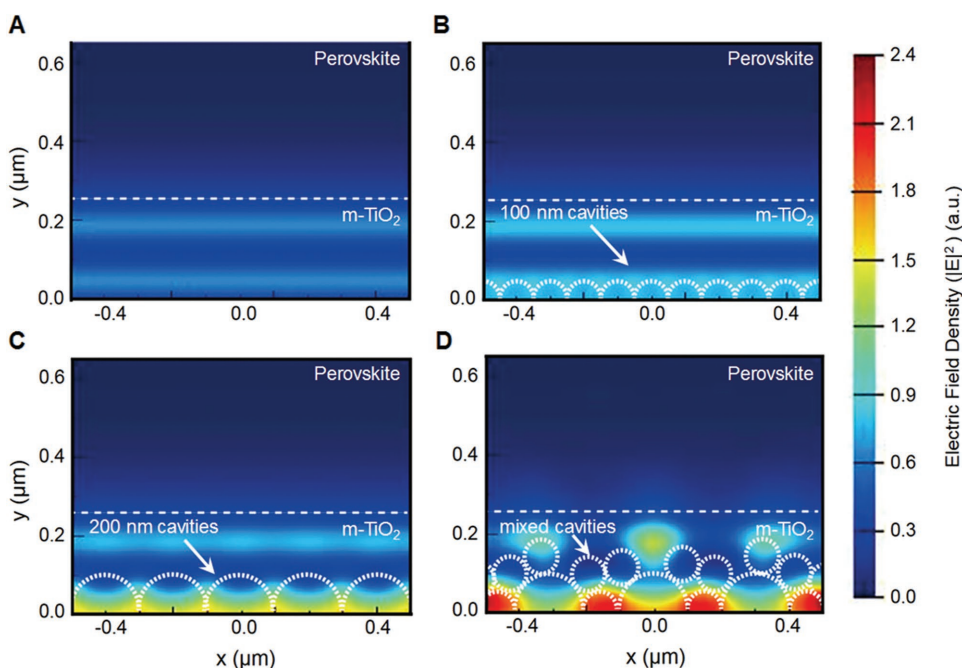

Figure 4. The spatial distribution of the light-driven electromagnetic (EM) field distribution within the SCL/m-TiO$_2$/CH$_3$NH$_3$PbI$_3$ architecture with A) control (w/o SCL), B) SCL-100, C) SCL-200, and D) SCL-MIX, where the incident plane EM wave of 500 nm < λ < 800 nm is given along the **y**-axis.

the SCL-MIX plays a key role in forming a strong standing wave in the m-TiO$_2$ layer, thus giving superior light-trapping capability for both the short- and long-wavelength regions. Consequently, this light-trapping capability is determined to enable broadband absorption of visible light on the perovskite layer without increasing its thickness. We also find that the light-driven standing wave gives enhanced charge extraction from the perovskite absorber layer with an increase of the shunt resistance (R_{sh}) for the photovoltaic cells with SCL-MIX (Table S1, Supporting Information).

The time-resolved PL decay measurements[33–35] have been also performed to investigate the charge-transfer kinetics of photogenerated charge carriers in the perovskite photovoltaic cell with SCLs, as shown in **Figure 5**A. The PL decay is fitted using the following triexponential equation:

$$y(t) = y_0 + \Sigma_i A_i \exp(-t/\tau_i) \quad (i = 1,2,3) \quad (3)$$

where A_i is a time-independent amplitude coefficient, τ_i is a decay time constant, and y_0 is a baseline constant. The fitted parameters are summarized in Table S2 (Supporting Information). The PL decay has been determined with the FTO/SCL/m-TiO$_2$/perovskite/spiro-OMeTAD architecture. The decay kinetics have been explored by determining the electron extraction capability with the spiro-OMeTAD hole quencher. We find that the average PL decay time constant (τ_{ave}) of the cell with SCL-MIX decreases to 0.77 ns, which is much shorter than the value (1.29 ns) for the control cell. This

supports that faster electron extraction has been achieved on the SCL-MIX by the enhanced light-driven EM field that promotes extraction of electrons. Furthermore, transient open-circuit photovoltage decay (OCPD) measurements have been used to explore charge recombination dynamics, as shown in Figure 5B.[36] When the light is switched off, the photovoltage of a photovoltaic cell is found to decrease with a first decay slope of –53.5 mV ms^{-1} for all the devices. However, the following decay slope of SCL-MIX (–0.94 mV ms^{-1}) was proven to be significantly smaller than –4.25 mV ms^{-1} for the control, –2.41 mV ms^{-1} for SCL-100, and –3.10 mV ms^{-1} for SCL-200. These results clarify that the increase in the carrier lifetime with SCL-MIX is due to its slowed recombination dynamics.

Furthermore, the electrochemical impedance spectroscopy (EIS) spectra at the open-circuit voltage condition under AM 1.5G illumination give more information on the carrier dynamics of photovoltaic devices.[35,37] The Nyquist plot (Figure 5C) shows one distinguishable asymmetric semicircle that can be fitted with the two resistor (R)–constant phase elements. The plots are fitted with the equivalent circuit, as shown in the inset of Figure 5C. We found that they are composed of three resistive components corresponding to series (R_S), charge transfer (R_{ct}), and recombination (R_{rec}). The R_{ct} is attributed to the resistance for electron extraction from the perovskite to m-TiO$_2$ since the structure for hole extraction is the same for all the devices and the resistance for hole extraction is similar. R_{ct} and R_{rec} correspond to high- and low-frequency elements,[35] respectively, and
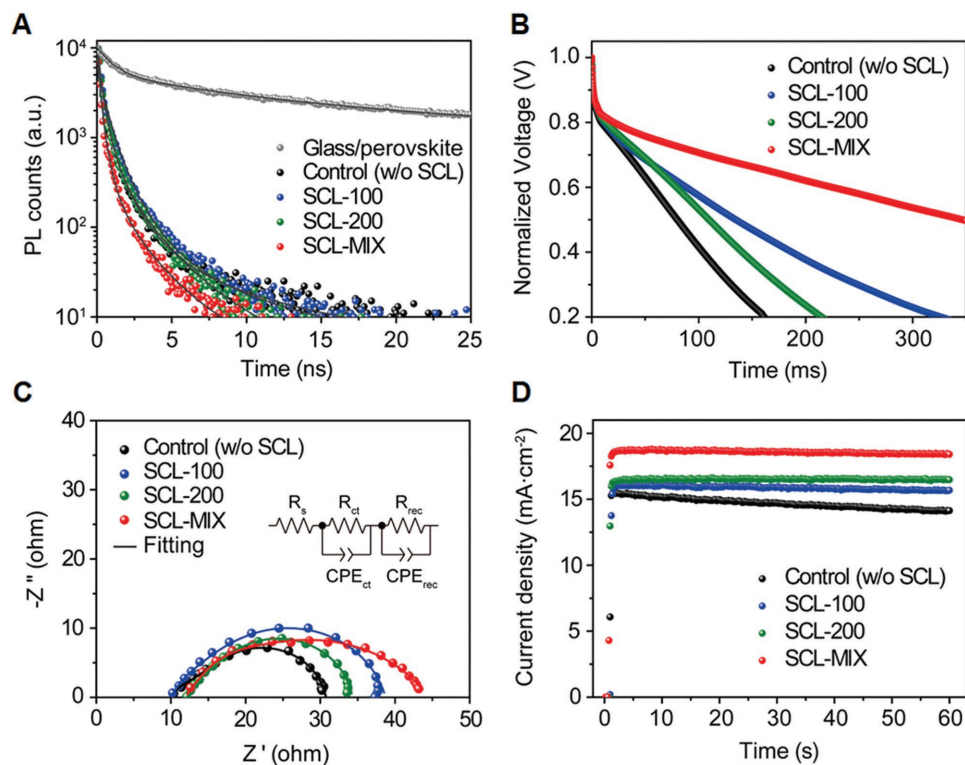

Figure 5. A) Time-resolved PL decay curves of the FTO/SCL/m-TiO$_2$/perovskite/spiro-OMeTAD, and B) transient open circuit photovoltage decay (OCPD) curves. C) Nyquist plots of electrical impedance spectra (EIS) measured at the open circuit voltage under AM 1.5G illumination (inset: equivalent circuit of the device, solid line: the fitting result) and D) transient current density of a device under AM 1.5G illumination.

the value of R_{ct} is found to decrease from 5.6 Ω (control) to 2.3 Ω (SCL-MIX), as summarized in Table S3 (Supporting Information). In addition, R_{rec} with SCL-MIX, corresponding to the resistance for recombination at the m-TiO$_2$/perovskite/spiro-OMeTAD interface, was increased to 30.3 Ω, which is substantially higher than 15.3 Ω with the control configuration. These results show that the stronger light-driven EM field existing in the SCL promotes electron extraction. In addition, we found that the EM field suppresses recombination at the interfaces of photovoltaic cells, thereby leading to the improved FF. Also, the transient current densities shown in Figure 5D showed stabilization of the current density of the photovoltaic cells under a continuous illumination condition.[33,35] When the photogenerated charge carriers accumulate at the trap states of the interfaces, the saturated photocurrent densities of the cells should decrease with time. The current density of a control cell is observed to decrease rapidly with time, while those of the photovoltaic cells with SCLs show stabilized current densities over time. These results indicate that the control cell suffers from charge accumulation in the interface of m-TiO$_2$ and the perovskite layer. However, we find that the photocurrent densities of the cells with SCLs are stabilized due to the fast electron extraction and the suppressed charge accumulation. Moreover, we find that the current density of the perovskite photovoltaic cell for SCL-MIX is restored to the initial value when the cell is reilluminated after having been kept in the dark.

In summary, we demonstrated that a new SCL, which is composed of mixed cavities of small (100 nm) and large (200 nm) size in a perovskite photovoltaic cell, enhances the light-absorption capability of the CH$_3$NH$_3$PbI$_3$ perovskite, and also enables efficient charge extraction from the perovskite absorber layer. The experimental studies and optical simulations proved that the mixed cavities enable broadband harvesting of all the photons in the short-wavelength ($\lambda < 500$ nm) and long-wavelength (500 nm $< \lambda < 800$ nm) regions for visible light. Moreover, it was demonstrated that SCL-MIX yields significantly increased current density. Furthermore, the results showed that a light-driven EM field is built in the SCL, thus enabling efficient charge extraction of electron–hole pairs produced upon light absorption. The EIS analysis further clarified that the light-driven EM field promotes electron extraction, while the suppressed recombination leads to an improved FF. In addition, the photovoltaic cell with the SCL-MIX device provided stabilized current density over time, which is attributed to fast charge transfer and suppressed charge accumulation. Consequently, we believe that the proposed SCL composed of mixed pore cavities could provide a new route to realize efficient harvesting of short- and long-wavelength photons in perovskite photovoltaic cells, as well as efficient charge separation of electron–hole pairs upon light absorption and improved stability over time.

Experimental Section

Optical Simulation: The optical simulations for the light-absorption density and the light-driven EM field density in the SCL/m-TiO$_2$/perovskite architecture with and without SCLs were performed using the FDTD (Lumerical) method with optical properties of materials including refractive indexes and extinction coefficients.[29,30] The plane-wave source was given along with the *y*-axis, and the wavelength ranges for simulation to explore the short- and long-wavelength regions of visible light were based on 350 nm $< \lambda < 500$ nm and 500 nm $< \lambda < 800$ nm, respectively. Also, the boundary condition for the *y*-axis was defined as a perfectly matched layer to specify the optical properties of the layer, on the open boundary that could absorb the incident EM wave. For the *x*- and *z*-axes, periodic boundary conditions were used so that the identical structure is repeated into the infinite space.

Fabrication of Photovoltaic Cells: The fluorine-doped tin oxide (FTO, TEC15, 15 Ω sq^{-1}, Pilkington) was sequentially rinsed by deionized water, ethanol, and acetone in the ultrasonication bath and treated by UV-ozone to remove organic residues. The 50 nm thick compact layer was prepared by spin-coating with 0.3 M titanium diisopropoxide bis(acetylacetonate) solution (75 wt% in isopropanol, Sigma-Aldrich, Saint Louis, USA) in 1-butanol (99.9%, Sigma-Aldrich) and annealed at 500 °C for 90 min. Four different types of perovskite photovoltaic cells without a SCL were prepared corresponding to the (1) control (w/o SCL), and with SCLs corresponding to the (2) SCL-100 and (3) SCL-200 prepared using the average size of 100 or 200 nm, respectively, for cavities, and (4) SCL-MIX having the mixed cavities of 100 and 200 nm. To fabricate SCL-100 and SCL-200, polystyrene nanospheres of 100 and 200 nm in sizes were spin-coated at 2000 rpm for 60 s using the polystyrene solution (polystyrene latex microsphere, 2.5 wt% dispersion in distilled water, Alfa-Aesar) diluted with ethanol (1:3 v/v) to fabricate layers of polystyrene spheres. Subsequently, the substrate was annealed at 70 °C for 5 min to evaporate the solvents and to form dense nanosphere array. In addition, for SCL-MIX, the mixture of 100 and 200 nm nanospheres was used using the ratio of nanospheres optimized to 3:7 (v/v). Then, 40×10^{-3} M TiCl$_4$ (99%, Junsei chemicals) aqueous solution was spin-coated on the polystyrene template to fill the pores of polystyrene layer and fabricate the SCL followed by annealing at 70 °C for 5 min. Next, TiO$_2$ nanoparticles were spin-coated at 2000 rpm for 60 s to form the mesoporous TiO$_2$ (m-TiO$_2$) layer using the commercial paste (18NR-T, Dyesol) diluted by ethanol (2:7 w/w). After that, the substrate was slowly heated to 500 °C and calcinated for 90 min to remove the polystyrene template. Additionally, an additional TiCl$_4$ (40×10^{-3} M) treatment was applied onto the substrate by the chemical bath deposition at 70 °C for 10 min and annealed at 500 °C for 30 min. Next, the 200 nm thick lead iodide layer was spin-coated at 6000 rpm for 30 s with 1 M PbI$_2$ (99.999%, Sigma-Aldrich) solution in anhydrous N,N-dimethylformamide (99.8%, Sigma-Aldrich) and dimethyl sulfoxide (99.9%, Sigma-Aldrich), and annealed on the hotplate at 65 °C for 1 min. Then, the perovskite (CH$_3$NH$_3$PbI$_3$) absorber layer was prepared through spin-coating of 10 mg mL^{-1} methyl ammonium iodide (99.5%, Lumtec) solution in isopropanol at 2000 rpm and annealed at 100 °C for 2 min. Also, the 200 nm thick hole transport layer was spin-coated at 4000 rpm for 30 s using the spiro-OMeTAD solution and oxidized in the desiccator for 12 h. The solution was prepared by dissolving 72.3 mg of 2,2′,7,7′-tetrakis(N,N′-di-p-methoxyphenylamine)-9,9′-spirobifluorene (99.5%, Lumtec), 28.8 µL of 4-tert-butylpyridine (96%, Sigma-Aldrich), 17.5 µL of a stock solution having

lithium bis(trifluoromethylsulphonyl)imide (99.95%, Sigma-Aldrich), and acetonitrile (520 mg mL^{-1}) in 1 mL of anhydrous chlorobenzene (99%, Sigma-Aldrich). Finally, the 100 nm thick patterned Au electrode was deposited with the metallic shadow mask under high vacuum using the thermal evaporator.

Characterization: The surface and cross-sectional morphologies were determined with the FE-SEM using Nova 230 (FEI company). Meanwhile, current density–voltage (*J–V*) curves of photovoltaic cells were measured with the potentiostat (Compactstat, IVIUM) under the simulated AM 1.5G (100 mW cm^{-2}, Newport Oriel) and the active area was controlled to 0.105 cm^2 with the metallic shadow mask. The EQE was determined with the spectrometer measurement system (PEC-S20, Peccell) and the power of the lamp was calibrated with the silicon reference cell. Moreover, the steady-state PL spectra were obtained using the 514 nm laser using the high-resolution PL spectrometer (LabRAM HR Evolution Visible-NIR, HORIBA). The time-resolved PL decay spectra were obtained using the fluorescence lifetime spectrometer (FL920, Edinburgh Instruments) and the 470 nm laser was used for excitation to collect the photons at 760 nm. In addition, the XRD patterns of TiO$_2$ films were obtained using the X-ray diffractometer (Cu Kα, D/MAX-2500, RIGAKU), while the absorbance and reflectance spectra on FTO/SCL/m-TiO$_2$/perovskite configuration were determined using the UV–vis spectrometer (Cary 300, Agilent technologies). Also, the EIS were obtained using the potentiostat (Compactstat, IVIUM) and the data were collected in a frequency range from 1 MHz to 100 Hz at the open-circuit potential under an irradiation of 100 mW cm^{-2}. The obtained spectra were determined through the Nyquist plots fitted with two semicircles with the high-frequency element corresponding to electron extraction from the perovskite to m-TiO$_2$ as well as the low-frequency element corresponding to recombination in the perovskite. Furthermore, the transient OCPD and current density decay plots were obtained using the potentiostat (SP-200, BioLogic Scientific) with the 500 W Xenon lamp (Newport).

Supporting Information

Supporting Information is available from the Wiley Online Library or from the author.

Acknowledgements

Conflict of Interest

The authors declare no conflict of interest.

[1] H. S. Kim, C. R. Lee, J. H. Im, K. B. Lee, T. Moehl, A. Marchioro, S. J. Moon, R. Humphry-Baker, J. H. Yum, J. E. Moser, M. Gratzel, N. G. Park, *Sci. Rep.* **2012**, *2*, 591.

[2] J. Burschka, N. Pellet, S. J. Moon, R. Humphry-Baker, P. Gao, M. K. Nazeeruddin, M. Gratzel, *Nature* **2013**, *499*, 316.

[3] N. J. Jeon, J. H. Noh, Y. C. Kim, W. S. Yang, S. Ryu, S. I. Seok, *Nat. Mater.* **2014**, *13*, 897.

[4] N. J. Jeon, J. H. Noh, W. S. Yang, Y. C. Kim, S. Ryu, J. Seo, S. I. Seok, *Nature* **2015**, *517*, 476.

[5] M. A. Green, A. Ho-Baillie, H. J. Sniath, *Nat. Photonics* **2014**, *8*, 506.

[6] S. D. Stranks, G. E. Eperon, G. Grancini, C. Menelaou, M. J. P. Alcocer, T. Leijtens, L. M. Herz, A. Petrozza, H. J. Snaith, *Science* **2013**, *342*, 341.

[7] A. Miyata, A. Mitioglu, P. Plochocka, O. Portugall, J. T. S. Wang, S. D. Stranks, H. J. Snaith, R. J. Nicholas, *Nat. Phys.* **2015**, *11*, 582.

[8] K. Hwang, Y. S. Jung, Y. J. Heo, F. H. Scholes, S. E. Watkins, J. Subbiah, D. J. Jones, D. Y. Kim, D. Vak, *Adv. Mater.* **2015**, *27*, 1241.

[9] Q. Lin, A. Armin, P. L. Burn, P. Meredith, *Nat. Photonics* **2015**, *9*, 687.

[10] Q. Lin, A. Armin, R. C. R. N. Nagiri, P. L. Burn, P. Meredith, *Nat. Photonics* **2014**, *9*, 106.

[11] T. G. Mayerhoffer, H. Mutschke, J. Popp, *ChemPhysChem* **2016**, *17*, 1948.

[12] S. D. Stranks, G. E. Eperon, G. Grancini, C. Menelaou, M. J. P. Alcocer, T. Leijtens, L. M. Herz, A. Petrozza, H. J. Snaith, *Science* **2013**, *342*, 341.

[13] G. Xing, N. Mathews, S. Sun, S. S. Lim, Y. M. Lam, M. Gratzel, S. Mhaisalkar, T. C. Sum, *Science* **2013**, *342*, 344.

[14] M. L. Brongersma, Y. Cui, S. Fan, *Nat. Mater.* **2014**, *13*, 451.

[15] Y. Yao, J. Yao, V. K. Narasimhan, Z. Ruan, C. Xie, S. Fan, Y. Cui, *Nat. Commun.* **2012**, *3*, 664.

[16] C. Battaglia, C. M. Hsu, K. Soderstrom, J. Escarre, F. J. Haug, M. Charriere, M. Boccard, M. Despeisse, D. T. L. Alexander, M. Cantoni, Y. Cui, C. Ballif, *ACS Nano* **2012**, *6*, 2790.

[17] K. X. Wang, Z. Yu, V. Liu, Y. Cui, S. Fan, *Nano Lett.* **2012**, *12*, 1616.

[18] Q. Zhang, D. Myers, J. Lan, S. A. Jenekhe, G. Cao, *Phys. Chem. Chem. Phys.* **2012**, *14*, 14982.

[19] S. J. Ha, J. H. Moon, *Sci. Rep.* **2014**, *4*, 5375.

[20] M. Y. Hsieh, F. I. Lai, W. C. Chen, M. C. Hsieh, H. Y. Hu, P. Yu, H. C. Kuo, S. Y. Kuo, *Nanoscale* **2016**, *8*, 5478.

[21] S. H. Lin, Y. H. Su, H. W. Cho, P. Y. Kung, W. P. Liao, J. J. Wu, *J. Mater. Chem. A* **2016**, *4*, 1119.

[22] J. W. Lee, S. H. Lee, H. S. Ko, J. Kwon, J. H. Park, S. M. Kang, N. Ahn, M. Choi, J. K. Kim, N. G. Park, *J. Mater. Chem. A* **2015**, *3*, 9179.

[23] J. Yin, H. Qu, J. Cao, H. Tai, J. Li, N. Zheng, *RSC Adv.* **2016**, *6*, 24596.

[24] S. M. Kang, S. Jang, J. K. Lee, J. Yoon, D. E. Yoo, J. W. Lee, M. Choi, N. G. Park, *Small* **2016**, *12*, 2443.

[25] W. Zhang, M. Saliba, S. D. Stranks, Y. Sun, X. Shi, U. Wiesner, H. J. Snaith, *Nano Lett.* **2013**, *13*, 4505.

[26] Z. Zhu, Y. Zho, W. Hu, Y. Li, Y. Gu, B. Cao, N. Guo, L. Wang, J. Song, S. Zhang, H. Gu, H. Zeng, *Adv. Funct. Mater.* **2016**, *26*, 1793.

[27] L. Yue, B. Yan, M. Attridge, Z. Wan, *Sol. Energy* **2016**, *124*, 143.

[28] M. Saliba, W. Zhang, V. M. Burlakov, S. D. Stranks, Y. Sun, J. M. Ball, M. B. Johnston, A. Goriely, U. Wiesner, H. J. Snaith, *Adv. Funct. Mater.* **2015**, *25*, 5038.

[29] E. D. Palik, *Handbook of Optical Constants of Solids*, Academic Press, Cambridge, MA, USA **1985**.

[30] P. Loper, M. Stuckelberger, B. Niesen, J. Werner, M. Filipic, S. J. Moon, J. H. Yum, M. Topic, S. D. Wolf, C. Ballif, *J. Phys. Chem. Lett.* **2015**, *6*, 66.

[31] R. Korlacki, R. F. Saraf, S. Ducharme, *Appl. Phys. Lett.* **2011**, *99*, 153112.

[32] V. Roiati, E. Mosconi, A. Listorti, S. Colella, G. Gigli, F. D. Angelis, *Nano Lett.* **2014**, *14*, 2168.

[33] J. H. Heo, M. S. You, M. H. Chang, W. Yin, T. K. Ahn, S. J. Lee, S. J. Sung, D. H. Kim, S. H. Im, *Nano Energy* **2015**, *15*, 530.

[34] G. Xing, B. Wu, S. Chen, J. Chua, N. Yantara, S. Mhaisalkar, N. Mathews, T. C. Sum, *Small* **2015**, *11*, 3606.

[35] D. Yang, X. Zhou, R. Yang, Z. Yang, W. Yu, X. Wang, C. Li, S. F. Liu, R. P. H. Chang, *Energy Environ. Sci.* **2016**, *9*, 3071.

[36] B. A. Nejand, S. Gharibzadeh, V. Ahmadi, H. R. Shahverdi, *Sci. Rep.* **2016**, *6*, 33649.

[37] J. Chen, Y. Rong, A. Mei, Y. Xiong, T. Liu, Y. Sheng, P. Jiang, L. Hong, Y. Guan, X. Zhu, X. Hou, M. Duan, J. Zhao, X. Li, H. Han, *Adv. Energy Mater.* **2015**, *6*, 1502009.